

Noname manuscript No.
(will be inserted by the editor)

**1 Significant wind disturbances induced by giant
2 dunes.**

**3 Cyril Gadal · Pauline Delorme ·
4 Clément Narteau · Giles Wiggs ·
5 Matthew Baddock · Joanna M. Nield ·
6 Philippe Claudin**

7
8 Received: DD Month YEAR / Accepted: DD Month YEAR

9 Abstract

10 abstract

11 Keywords Boundary layer · Turbulent flow · Sand dunes · Fluide-structures
12 interactions

C. Gadal

Institut de Mécanique des Fluides de Toulouse (IMFT), Université de Toulouse, CNRS,
INPT, UPS, Toulouse, France
E-mail: cyril.gadal@imft.fr

S. Author
second address

T. Author
third address

13 1 Introduction

14 Whenever a flow encounters an obstacle, various types of interactions can arise
15 depending on the different time and length scales involved. In the case of atmo-
16 spheric flows, this depends mainly on the part of the vertical structure of the
17 atmosphere, schematically composed of a turbulent boundary layer topped by
18 a turbulence-free part, with which the obstacle interacts (Stull 1988). At the
19 largest scale, the feedback of mountains on the stratified flow of the free at-
20 mosphere results in wave generation as well as significant wind disturbances,
21 such as foehn winds in the lee side (?). Inside the boundary layer, the inter-
22 action between a turbulent flow and hilly surfaces is for example key to the
23 understanding ocean surface wind-driven waves, or eolian bedforms in desert
24 (Belcher and Hunt 1998; Sullivan and McWilliams 2010; Courrech du Pont
25 2015).

26 Indeed, eolian sand dunes typically emerge from the feedback of the topog-
27 raphy on the turbulent flow, which speeds up close to the dune crest (Rubin
28 and Hunter 1987; Charru et al. 2013; Courrech du Pont et al. 2014). Later
29 on, when the dune reaches an intermediate size, it may also induce significant
30 wind deflections. This can impact the sediment pathways of coastal systems
31 (Hesp et al. 2015), or affect the collective behavior of dune populations with
32 long-range interactions due to flow disturbances induced by each individual
33 (Smith et al. 2017; Bacik et al. 2020). As the dunes increase in size by col-
34 lisions and coarsening, they sometimes reach a giant size, comparable to the
35 boundary layer depth, thus inducing interactions not only with the turbulent
36 flow of the ABL, but also with the free atmosphere (Andreotti et al. 2009).
37 However, the wind disturbances induced by these giant dunes have never been
38 quantified.

39 The study of the impact of obstacles on the atmospheric flows allows its
40 incorporation within meteorological numerical model. Therefore, they mainly
41 become limited by the precision of the included topographical data, as well
42 as the spatial grid of the model. For example, the latest climate reanalysis,
43 ERA5-Land, is limited by its 9 km spatial resolution, while including the
44 data 30-m Digital Elevation Models (DEMs) of the shuttle radar topography
45 mission (Farr et al. 2007; Muñoz-Sabater et al. 2021). As such, it can not
46 reproduce the flow disturbances induced by giant dunes, which have a typical
47 length scale ~ 1 km.

48 Here, we compare the wind predictions from the ERA5-Land dataset to
49 local measurements in four different places across the Namib desert. In places
50 with no significant topographies smaller than the model grid, we show that
51 both wind datasets agree with each other. On the contrary, in places with
52 giant dunes, we show that they may differ for some specific meteorological
53 conditions, that we link to the circadian cycle of the ABL. We thus highlight
54 the importance of the mid-scale topographies for local wind regimes, and its
55 implications in the case of sand seas for smaller-scale eolian bedforms.

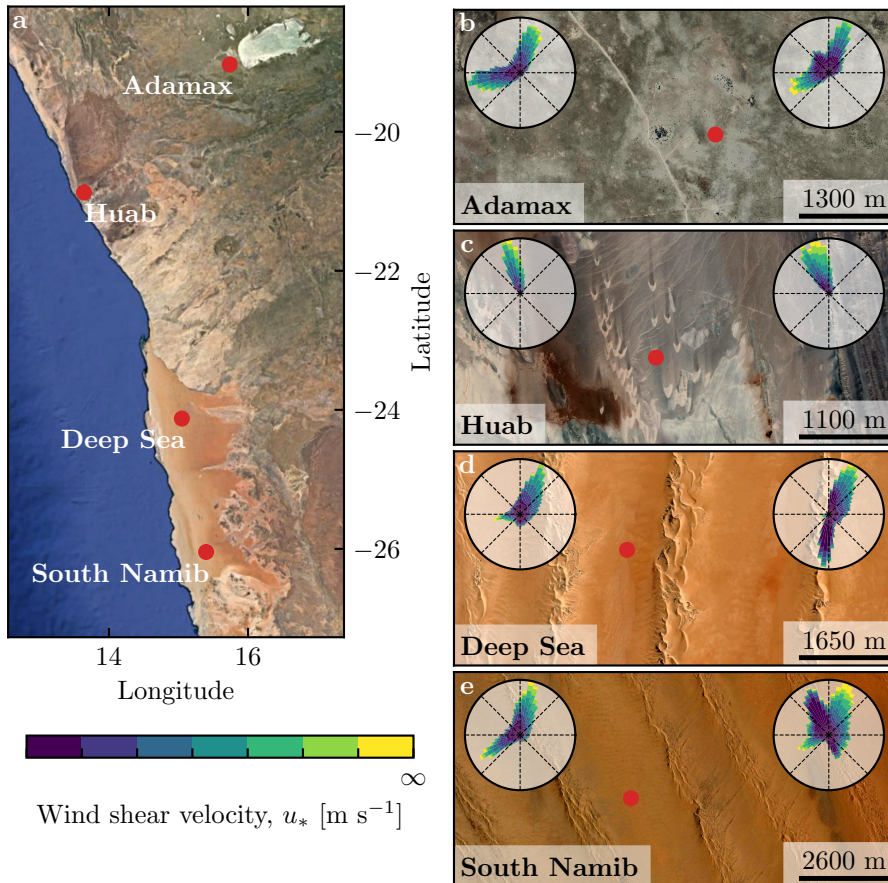


Fig. 1 Wind data used in this study **a**: Location of the studied sites. **b–e**: Satellite images of the studied sites (Google-Earth, Maxar Technologies, CNES/Airbus). In each subplot, the left and right wind roses represent the data from the ERA5Land climate reanalysis and the local wind stations, respectively. Note that the bars show the direction towards which the wind blows. The red dots show the location of local wind stations.

56 2 Wind regimes across the Namib Sand Sea

57 In this study, we focus on four places across and nearby the Namib desert,
 58 highlighting different environments (see Fig. 1). The Adamax station is lo-
 59 cated near the Adamax salt pan, in a highly vegetated area. The Huab station,
 60 located on the coast at the outlet of the Huab river is an arid environment
 61 exhibiting 60-m scale barchan dunes. While these two stations are in environ-
 62 ments with no mid-scale topography, this is not the case for the Deep Sea
 63 and South Namib stations. Both are located in the interdune between giant
 64 linear dunes with kilometric wavelengths and superimposed patterns. In this
 65 section, we describe and compare the wind regimes resulting from the available
 66 datasets in each station.

67 2.1 Datasets

68 Two wind datasets are used in this study. First, local winds are provided by
 69 stations situated in the four different places (see Fig. 1). The wind strength and
 70 direction are measured every 10 minutes by cup anemometers and wind vanes,
 71 at heights between 2 m and 3 m depending on the station. The available period
 72 of measurements ranges from 1 to 5 discontinuous years distributed between
 73 2012 and 2020 (see Fig. S1). We checked that at least one complete seasonal
 74 cycle is available at each station. Then, regional winds are extracted at the
 75 same locations and periods from the ERA5-Land dataset, which is a replay
 76 at a smaller spatial resolution of ERA5, the latest climate reanalysis from
 77 the ECMWF (Hersbach et al. 2020; Muñoz-Sabater et al. 2021). It provides
 78 hourly estimates of the 10-m wind velocity and direction at a spatial resolution
 79 of ~ 9 km ($0.1^\circ \times 0.1^\circ$).

80 For comparison, the local measurements are averaged into 1-hr bins cen-
 81 tered on the temporal scale of the ERA5-Land estimates (see Fig. S2). As the
 82 wind velocities of both datasets are provided at different heights, we convert
 83 them into shear velocities (see SI section 1), characteristic of the whole turbu-
 84 lent wind profile within the atmospheric boundary layer, which are then used
 85 together with the wind direction for further analysis. The resulting wind data
 86 are shown on the wind roses of Fig. 1(b–e).

87 Finally, the dune properties are computed using autocorrelation on the 30-
 88 m Digital Elevation Models (DEMs) of the shuttle radar topography mission
 89 (Farr et al. 2007). For the South Namib and Deep Sea stations, we obtain
 90 respectively orientations of 85° and 125° , wavelengths of 2.6 km and 2.3 km
 91 and amplitudes of 45 m and 20 m (see Fig. S4 for more details).

92 2.2 Agreement between local and regional winds

93 The obtained wind regimes are shown in figure 1. In the Namib, the regional
 94 wind patterns are essentially controlled by the sea breeze, resulting in strong
 95 northward components (sometimes slightly deviated by the large scale topogra-
 96 phy) present in all regional wind roses (Lancaster 1985). These daily winds are
 97 dominant during the second-half of the year (Septembre-January). In winter,
 98 an additional easterly component can be recorded during the night, induced by
 99 the combination of katabatic winds forming on the mountains, and infrequent
 100 ‘berg’ winds, which are responsible of the high wind velocities observed (Lan-
 101 caster 1984). The frequency of these easterly components decreases from the
 102 inland to the coast, resulting in bidirectional wind regimes within the Namib
 103 Sand Sea and at the Adamax salt pan (Fig. 1b, 1d and 1e) and a unidirectional
 104 wind regime on the coast at the outlet of the Huab River (Fig. 1c).

105 In the case of the Adamax and Huab stations, the regional wind roses
 106 qualitatively match those corresponding to the local in situ measurements.
 107 However, for the Deep Sea and South Namib stations, the local wind roses
 108 exhibit additional components aligned with the giant dune orientation visible

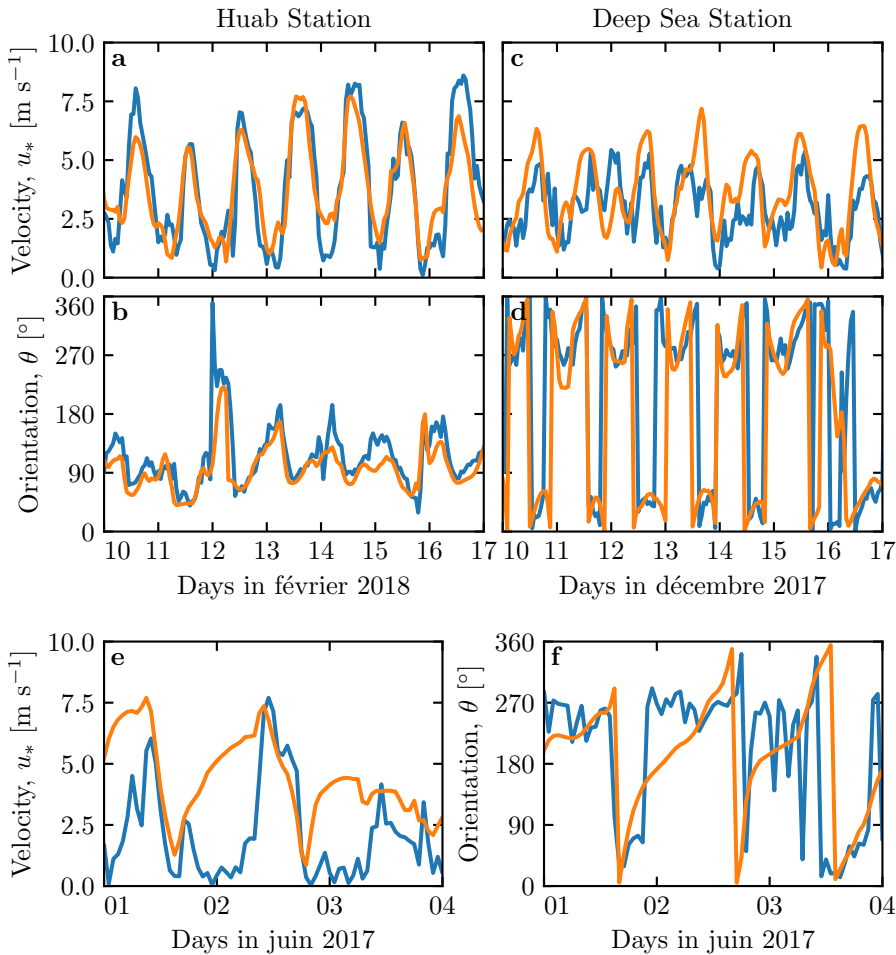


Fig. 2 Temporal comparison between the wind data coming from the Era5Land climate reanalysis (orange lines) and from the local measurements (blue lines). **a–b:** Huab station. **c–d:** Deep Sea station in winter. **e–f:** Deep Sea station in summer.

on the satellite images (Fig. 1c–d). Indeed, the analysis of the wind speed and direction time series shows that the agreement between the local and regional datasets is always verified when no mid-scale topography are present (Fig. 2a–b) and Fig. S5). In contrast, for the stations within the giant dune field, we observe that this agreement is limited to the Septembre–January time periods (Fig. 2c–d).

2.3 Influence of the giant dunes on local wind regimes

When giant dunes are present, in the February–August period, the local and regional winds match only during the morning, i.e when the southerly/southwesterly

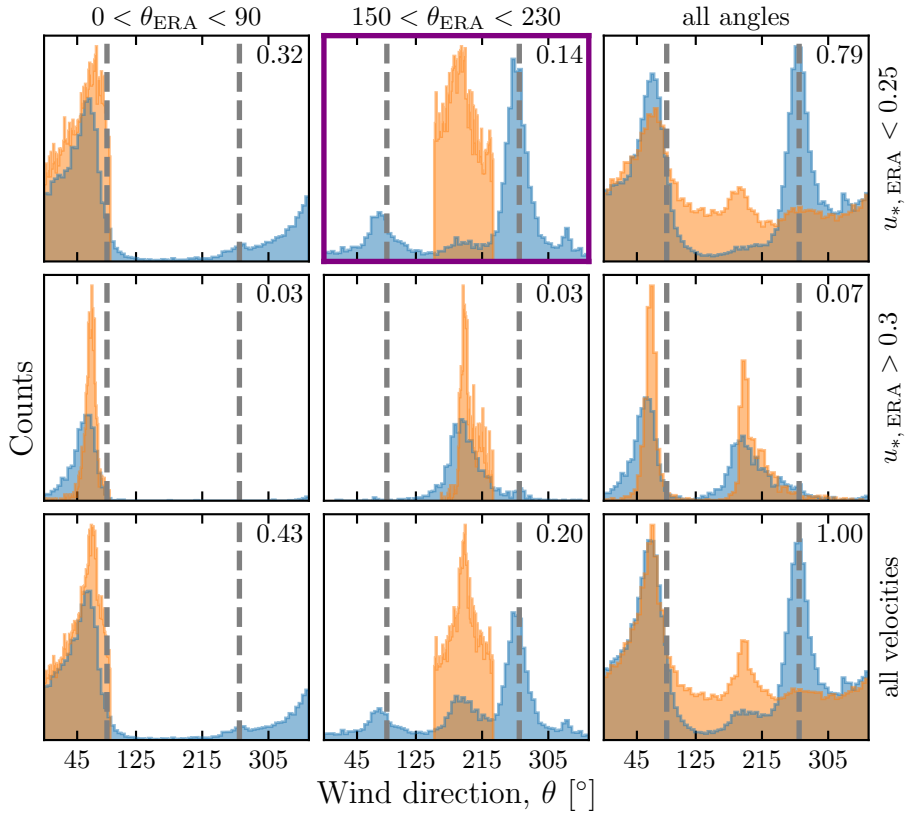


Fig. 3 Distributions of wind direction at the Deep Sea Station for the Era5Land climate reanalysis (orange) and the local measurements (blue). In each subplot, both distributions are plotted from the same time steps, selected with constraints on the wind direction (columns) and/or wind velocity (rows) of the Era5Land dataset. The gray vertical dashed lines indicate the dune orientation, and the top right numbers the percentage of the total number of time steps selected in each subplot. The purple frame highlights the regime (small wind velocities, nocturnal summer wind) in which the data from both datasets differs. A similar figure can be obtained for the Deep Sea station (see Fig. S6).

118 sea breeze dominates (see Fig. 2(e–f), Fig. 3 and Fig. S6). In the late after-
 119 noon and during the night, when the northwesterly ‘berg’ and katabatic winds
 120 blow, the two datasets differ. In this case, the angular wind distribution of
 121 the local measurements exhibits two additional modes separated of $\simeq 180^\circ$,
 122 each corresponding to the giant dune alignment (purple frame in Fig. 3 and
 123 Fig. S6, as well as Fig. S7). This deviation is also associated with a global
 124 attenuation of the wind strength (Fig. S8). Remarkably, all these figures show
 125 that this process occurs for low wind velocities, typically for $u_* < 0.1 \text{ m s}^{-1}$.
 126 For shear velocities larger than 0.25 m s^{-1} , this wind reorientation does not
 127 occur. Finally, for intermediate shear velocities, both reorientation along the
 128 dune crest and no reorientation are observed (Fig. S7).

129 **3 Influence of the circadian cycle of the atmospheric boundary
130 layer**

131 In the case of linear ridges, dune-induced flow disturbances have mainly been
132 related to the incident wind direction (Walker et al. 2009; Hesp et al. 2015).
133 In our case, it is unlikely to be the dominant parameter, as the most deflected
134 wind for both stations is the most perpendicular, where it should be winds
135 with incident directions between 30° and 70° (Hesp et al. 2015). An important
136 observation is the difference in behavior between low and high wind velocities,
137 which suggests a change in the hydrodynamical regime.

138 Previous studies have linked atmospheric flow around and over topographical
139 obstacles to the vertical structure of the atmosphere (Stull 1988). More
140 particularly, dunes evolves in its lower part, the turbulent atmospheric bound-
141 ary layer (ABL), typically characterized by a logarithmic wind profile and a
142 vertically constant potential temperature. Above, the free atmosphere (FA) is
143 a stably stratified zone in which turbulence is negligible, and where the flow
144 is usually considered as incompressible and inviscid. In the middle, a transi-
145 tional layer, also known as entrainment zone, is characterized by a sharp
146 increase of the potential temperature, which traps the turbulence resulting
147 from the surface friction below it.

148 In the following, we sum-up the dominant numbers leading to different
149 hydrodynamical interactions with topographical obstacles, and interpret the
150 data with respect to the corresponding physical mechanisms.

151 **3.1 Relevant non-dimensional parameters and physical modeling**

152 Flow deflection over ridges can be simplistically understood from a balance
153 between inertia and pressure gradients (Hesp et al. 2015). As the flow ap-
154 proaches the ridge crest, the compression of the streamlines results in larger
155 flow velocities, and thus lower pressures (Rubin and Hunter 1987). An incident
156 flow oblique to the ridge is then deflected towards lower pressure zones, i.e to-
157 wards the crest. Turbulent dissipation at the bottom and non-linearities tends
158 to increase this effect downstream, resulting in along the crest wind deflection
159 in the lee side (Hesp et al. 2015; Gadal et al. 2019).

160 Another way to increase the flow deflection is its confinement below a
161 capping surface, that results in further streamline compression. This happens
162 when the flow disturbance induced by the obstacle reaches the surface. As
163 obstacles typically disturb flow over a characteristic height similar to their
164 width, the potential of interaction between the dunes and the overlying atmo-
165 spheric structure is well captured by the parameter kH , where $k = 2\pi/\lambda$ is
166 the wavenumber and H the ABL depth. Here, the giant dunes have kilometric
167 wavelengths, such that $0.02 \lesssim kH \lesssim 5$, and they interact most of the time
168 with the capping layer and the stratified free atmosphere above (Andreotti
169 et al. 2009).

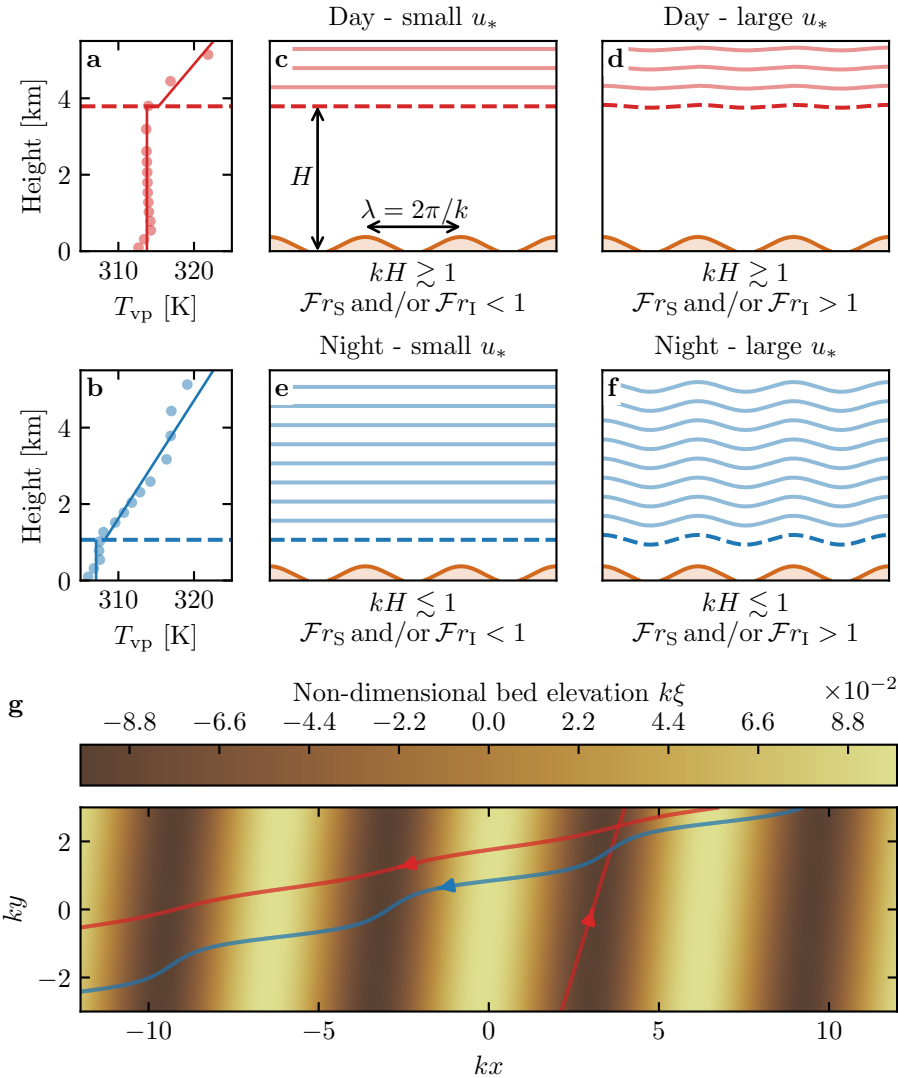


Fig. 4 **a–b:** Vertical profiles of the virtual potential temperature at 2 different time steps (blue - 29/11/2012 - 1100 UTC, red - 21/03/2017 - 1200 UTC) at the Deep Sea station. Dots: data from the ERA5 reanalysis. Transparent dashed lines: boundary layer height given by the ERA5 reanalysis, calculated from the bulk Richardson number (Seidel et al. 2012). Plain lines: vertical (boundary layer) and linear (free atmosphere) fits to estimate the stratification properties. **c–f:** Sketches representing the interaction between the giant dunes and the atmospheric flow for different meteorological conditions. **g:** Streamlines qualitatively representing the effect of flow confinement, in the case of the Deep Sea station. The red lines are calculated from the unconfined case similar to **d**. The sinuous blue line represents a confined case similar to **f**. For details on the streamline derivation, see Appendix 4.

170 Note that the ability of the capping layer and stratification to accommodate
 171 a perturbation induced by the topography directly impacts the strength of
 172 this confinement effect (Fig. 4). This is typically quantified using surface and
 173 internal Froude numbers (Vosper 2004; Stull 2006; Sheridan and Vosper 2006;
 174 Hunt et al. 2006; Jiang 2014):

$$\mathcal{Fr}_S = \frac{U}{\sqrt{\frac{\Delta\rho}{\rho} g H}}, \quad \mathcal{Fr}_I = \frac{kU}{N}, \quad (1)$$

175 where U is the wind velocity at the top of the ABL, ρ its average density, $\Delta\rho$
 176 the density jump between the ABL and the FA and N is the Brunt-Väisälä
 177 frequency, characteristic of the stratification.

178 The smallest wind disturbances are expected during the day, when the
 179 ABL depth is comparable to the dune wavelength ($kH \gtrsim 1$) and for large
 180 wind velocities, which correspond to a weak confinement situation (Fig. 4d).
 181 On the contrary, large wind disturbances are expected to occur during the
 182 night, when the confinement is mainly induced by shallow ABL (Fig. 4e–f).
 183 Note that this strong confinement can be somewhat reduced in the case of
 184 strong winds (corresponding to large Froude numbers, see Fig. 4f), explaining
 185 the threshold in velocity observed in the data (see section 2.3).

186 3.2 Flow regime diagrams

187 To highlight these different regimes from our data, we compute wind dis-
 188 turbance diagrams in the space defined by the three relevant non-dimensional
 189 numbers presented above, (kH , \mathcal{Fr}_S , \mathcal{Fr}_I). Those are calculated from the time
 190 series of the geopotential, temperature and specific humidity vertical profiles
 191 available in the ERA5 climate reanalysis (see SI section 2). Flow deviation is
 192 computed as the minimal angle between the wind orientations from the two
 193 datasets:

$$\delta_\theta = |\min([\theta_{\text{ERA}} - \theta_{\text{station}}] \bmod 360, [\theta_{\text{station}} - \theta_{\text{ERA}}] \bmod 360)|. \quad (2)$$

194 The relative velocity modulation is computed as

$$\delta_u = \frac{u_*^{\text{ERA}} - u_*^{\text{station}}}{u_*^{\text{ERA}}}. \quad (3)$$

195 As both Froude numbers have qualitatively the same impact on the flow
 196 confinement, we first leave aside the internal Froude number, and focus on
 197 the space (kH , \mathcal{Fr}_S). When representing the two variables δ_θ and δ_u in this
 198 space, different regime emerges (Fig. 5). Small wind disturbances ($\delta_\theta \rightarrow 0$,
 199 $\delta_u \rightarrow 0$) are located in the top-right part of the diagrams, corresponding
 200 to a regime mixing low-interaction and low-confinement (kH and \mathcal{Fr}_S large
 201 enough, Fig. 4d). Lower values of kH (stronger interaction) or Froude numbers
 202 (stronger confinement) then both leads to an increase in wind disturbances,

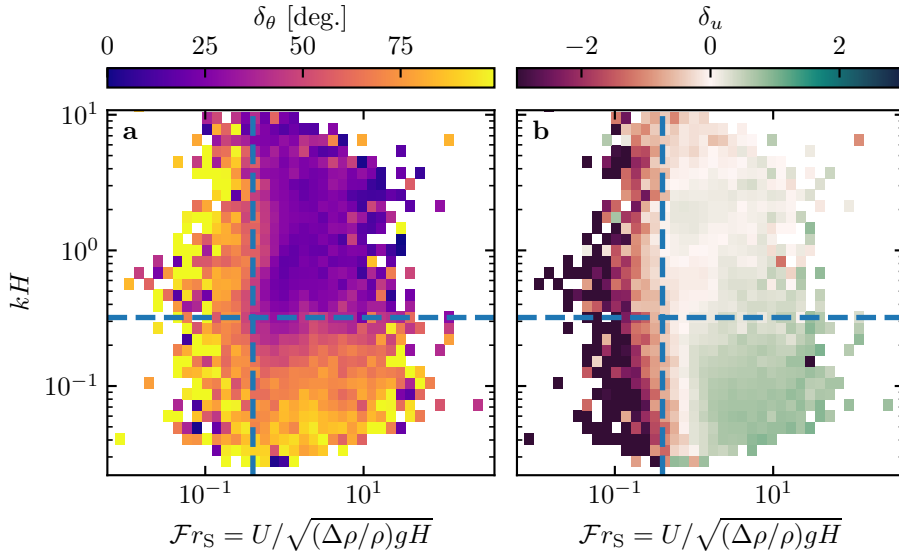


Fig. 5 Regime diagrams of the wind deviation δ_θ and relative attenuation/amplification δ_u in the space (\mathcal{Fr}_S, kH) , containing the data from both the Deep Sea and South Namib stations. Blue dashed lines empirically delimit the different regimes. The point density in each bin of the diagrams is shown in Fig. S11. The regime diagrams in the spaces (\mathcal{Fr}_I, kH) and $(\mathcal{Fr}_I, \mathcal{Fr}_S)$ are shown in Fig. S12.

both in terms of orientation and velocity. Below a threshold value of $kH \simeq 0.3$,
 203 wind disturbance occurs independently of the Froude numbers value. Furthermore,
 204 this also seems to control a transition between damped to amplified
 205 wind velocities within the interdune (Fig. 5b), for which we do not have an
 206 explanation. Note that the same interpretation can be done with the diagrams
 207 including the internal Froude number \mathcal{Fr}_I , as shown by Fig. S12.

Interestingly, the limit of no-interactions between the topography and the
 209 boundary layer structure ($kH \gg 1$), in which the properties of the capping
 210 layer and the stratification become irrelevant, is never reached here, in the
 211 case of giant dunes.
 212

213 4 Discussion

214 The comparison of local and regional wind data gives a direct evidence of the
 215 giant dunes feedback on the flow. In flat areas, the matching between both
 216 datasets highlights the ability of the latest generation of climate reanalysis to
 217 predict the wind flow up to scales ~ 10 km, i.e the grid model. When smaller
 218 scale topographies are present (giant dunes in our case), locally measured wind
 219 regimes may significantly differ from the regional ones. Furthermore, we link
 220 these disturbances induced by the dunes to their interaction with the lower
 221 part of the atmospheric vertical structure, and more specifically to its circa-
 222 dian variability. During the day, the top of the ABL is high enough to limit

the interaction of the capping layer and the FA stratification with the giant dunes, resulting in a low flow confinement, and thus small wind disturbances. During the night, the small ABL height induces a stronger flow confinement, associated with large wind deviation and acceleration or deceleration. Interestingly, we also found that this effect could be counterbalanced by the presence of large wind velocities, capable of deforming the capping layer and/or the FA stratification and thus decreasing the confinement effect.

Simple linear model such as the one of Andreotti et al. (2009) also suggests that larger wind disturbances occur under strong flow confinement such as described above. However, they are unable to reproduce the magnitude of the observed deviations, probably due to the presence of hydrodynamical non-linear effects, negligible in low confinement situations, but not otherwise (see Fig. S12 and Appendix 1). Another limit in the comparison between theoretical predictions and measured is induced by the single-point measurements. To have reliable representations of the flow structures related to wind disturbances, additional measurements in different places on and near the same topographical obstacle are needed.

This study highlights the interaction between giant dunes and the atmospheric boundary layer, thus supporting for example the way the capping layer acts as a bounding surface limiting dune growth (Andreotti et al. 2009; Gunn et al. 2021). This interaction also has implications at smaller scales, where bedforms then develop from the disturbed wind instead of the regional one. Differences between larger and smaller scale (thus older and more recent) dune patterns are observed ubiquitously, and have sometimes in the literature been attributed to climatic changes in wind regimes (?). Here, we suggest using this feedback mechanism that current winds can explain dune patterns at all scales, such as the linear dunes (~ 50 m-wide) elongating within the interdune between two giant linear dunes (~ 2 km-wide) in the Namib Sand Sea (see Fig. 6).

Acknowledgements These should follow the concluding section of the paper and precede the References and any appendices, if they are present. The acknowledgements section does not require a section number.

Appendix 1: ABL turbulent wind model

Following the work of Fourriere et al. (2010) and Andreotti et al. (2012), we briefly expose in this section the linear response of a turbulent flow to a small aspect ratio perturbation of the topography ξ . As this topography can be decomposed into several sinusoidal modes, we focus on the response to a sinusoidal topography as:

$$\xi = \xi_0 \cos [k (\cos(\alpha)x + \sin(\alpha)y)], \quad (4)$$

which is also a good approximation to the giant dunes observed in the Deep Sea and South Namib Station (see Fig 1 and Fig S4). Here, x and y are

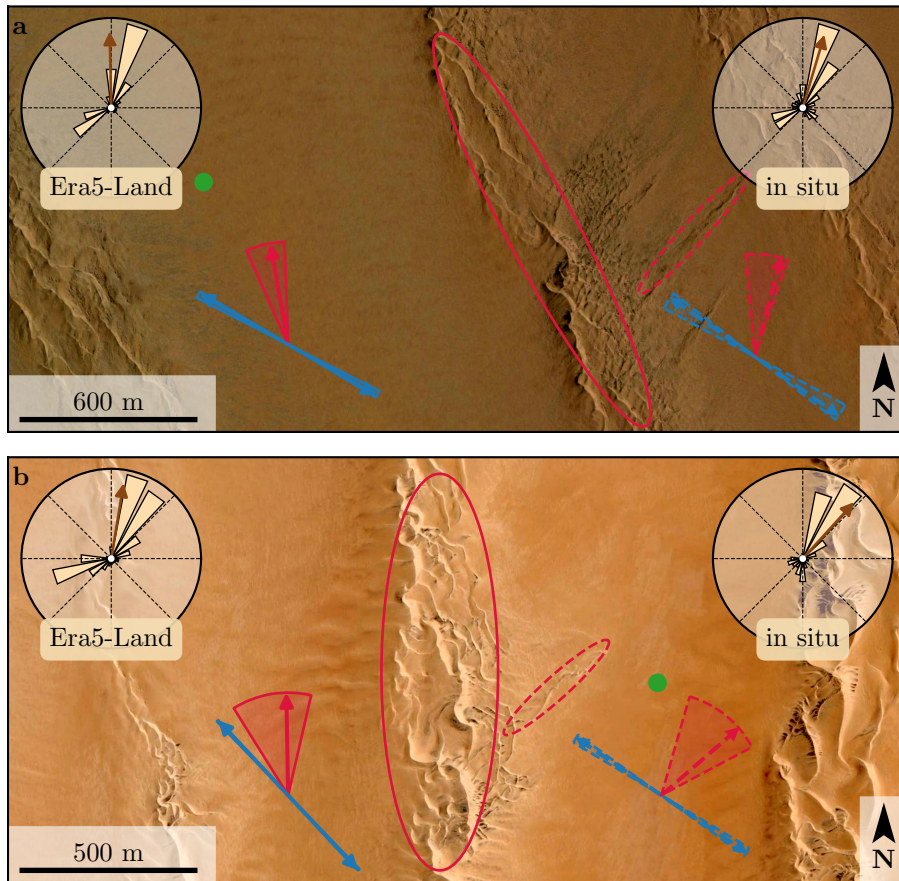


Fig. 6 Implications for smaller scale patterns in (a) the South Namib and (b) Deep Sea. The ellipses indicates the different types of elongating dunes, at large (plain) and small scale (dashed). The dune orientations are calculated using the model of Currech du Pont et al. (2014) from the sand flux angular distributions, shown here for typical sand quartz grains of $180\ \mu\text{m}$. The double blue and single red arrows correspond to the two possible dune growth mechanisms, bed instability and elongation, respectively. Likewise, plain arrows are calculated from the ERA5-Land datasets, and dashed arrows from the in situ measurements. Wedges show the uncertainty on the orientation calculation, and the arrows correspond to typical parameters found in the literature, i.e a grain diameter of $180\ \mu\text{m}$ and a flux-up ratio of 1.6. The green dots indicate the position of the measurement stations. See Appendix 2 for additional details.

263 the streamwise and spanwise coordinates, $k = 2\pi/\lambda$ the wavenumber of the
 264 sinusoidal perturbation, and α its crest orientation, calculated with respect to
 265 the y -direction.

²⁶⁶ In terms of basal shear stress $\tau = \rho u_*^2$, the flow response can then generally
²⁶⁷ be written in as:

$$\tau_x = \tau_0 \left(1 + k\xi_0 \sqrt{\mathcal{A}_x^2 + \mathcal{B}_x^2} \cos [k(\cos(\alpha)x + \sin(\alpha)y) + \phi_x] \right), \quad (5)$$

$$\tau_y = \tau_0 k \xi_0 \sqrt{\mathcal{A}_y^2 + \mathcal{B}_y^2} \cos [k(\cos(\alpha)x + \sin(\alpha)y) + \phi_y], \quad (6)$$

²⁶⁸ where τ_0 is the basal shear stress on a flat bed, and $\phi_{x,y} = \tan^{-1}(\mathcal{B}_{x,y}/\mathcal{A}_{x,y})$.
²⁶⁹ The in-phase and in-quadrature hydrodynamical coefficients $\mathcal{A}_{x,y}$ and $\mathcal{B}_{x,y}$
²⁷⁰ are functions of the flow conditions, i.e the bottom roughness, the free surface
²⁷¹ or the incident flow direction (Fourriere et al. 2010; Andreotti et al. 2009, 2012;
²⁷² Charru et al. 2013).

²⁷³ Andreotti et al. (2012) have shown that the impact of the incident wind
²⁷⁴ direction can be well approximated by the following expressions:

$$\mathcal{A}_x = \mathcal{A}_0 \cos^2 \alpha, \quad (7)$$

$$\mathcal{B}_x = \mathcal{B}_0 \cos^2 \alpha, \quad (8)$$

$$\mathcal{A}_y = \frac{1}{2} \mathcal{A}_0 \cos \alpha \sin \alpha, \quad (9)$$

$$\mathcal{B}_y = \frac{1}{2} \mathcal{B}_0 \cos \alpha \sin \alpha, \quad (10)$$

²⁷⁵ where \mathcal{A}_0 and \mathcal{B}_0 are now two coefficients independent of the dune orientation
²⁷⁶ α . In the case of a fully turbulent boundary layer capped by a free atmosphere
²⁷⁷ capping, they now only depend on kH , kz_0 , \mathcal{Fr}_I and \mathcal{Fr}_S , as detailed by
²⁷⁸ Andreotti et al. (2009). More specifically, their variation in the marginal spaces
²⁷⁹ (kH , \mathcal{Fr}_S) and (kH , \mathcal{Fr}_I) are shown in Fig. S12.

²⁸⁰ Typical values for the unconfined case are therefore $\mathcal{A}_0 = 3.4$ and $\mathcal{B}_0 = 1$.
²⁸¹ In our case of giant dunes with $k\xi_0 \sim 0.1$, significant wind disturbances are
²⁸² then expected when $\sqrt{\mathcal{A}_0^2 + \mathcal{B}_0^2} \sim 10$. However, this is also the limit of the
²⁸³ linear regime where this theoretical model is applicable, as hydrodynamical
²⁸⁴ non-linearities become significant when $k\xi_0 \sqrt{\mathcal{A}_0^2 + \mathcal{B}_0^2} \sim 1$.

²⁸⁵ Appendix 2: Sediment transport and dune morphodynamics

²⁸⁶ Here, we briefly detail the sediment transport and dune morphodynamics theo-
²⁸⁷ retorical framework leading to the prediction of sand fluxes and dune orientations
²⁸⁸ from wind data.

²⁸⁹ The sediment fluxes can been directly linked to the wind basal shear stress
²⁹⁰ at each time steps t from transport laws, whose exact forms depends on the
²⁹¹ sediment transport mechanisms taken into account. In this work, we following
²⁹² the recent work of Pähntz and Durán (2020), where the sediment flux q_{sat} on a
²⁹³ flat bed made of loose sand can be expressed as:

$$\frac{q_{\text{sat}, t}}{Q} = \frac{2\sqrt{\Theta_{\text{th}}}}{\kappa\mu} (\Theta_t - \Theta_{\text{th}}) \left(1 + \frac{C_M}{\mu} [\Theta_t - \Theta_{\text{th}}] \right), \quad (11)$$

where $\kappa = 0.4$ is the von Kármán constant, $C_M = 1.7$ a constant, $Q = d\sqrt{(\rho_s - \rho)gd/\rho}$ is a characteristic flux, with $\rho_s = 2.6 \text{ g cm}^{-3}$ and $d = 180 \mu\text{m}$ the grain density and diameter, and g the gravitational acceleration. The friction coefficient μ is taken to be the avalanche slope of the granular material, i.e. ~ 0.6 . Finally, the Shields number is defined as $\Theta = \rho u_{*,t}^2 / (\rho_s - \rho)gd$, and its threshold value for incipient sediment transport as been calibrated using laboratory experiments to $\Theta_{\text{th}} = 0.0035$.

The dune orientations are then predicted from the dimensional model of Courrech du Pont et al. (2014). The orientation α corresponding the bed instability is then the one that maximizes the following growth rate:

$$\sigma \propto \frac{1}{HWT} \int_t q_{\text{crest},t} |\sin(\theta_t - \alpha)|, \quad (12)$$

where H and W are dimensional constants representing the dune height and width, respectively. The flux at the crest is expressed as:

$$q_{\text{crest},t} = q_{\text{sat},t} [1 + \gamma |\sin(\theta_t - \alpha)|], \quad (13)$$

where the flux-up ratio γ has been calibrated to 1.6 using field studies, underwater laboratory experiments and numerical simulations. Similarly, the dune orientation corresponding to the elongation mechanism is the one that verifies:

$$\tan(\alpha) = \frac{\langle q_{\text{crest},t}(\alpha) \mathbf{e}_{\theta_t} \rangle \cdot \mathbf{e}_{WE}}{\langle q_{\text{crest},t}(\alpha) \mathbf{e}_{\theta_t} \rangle \cdot \mathbf{e}_{SN}}, \quad (14)$$

where $\langle . \rangle$ denotes a vectorial time average. The unitary vectors \mathbf{e}_{WE} , \mathbf{e}_{SN} and \mathbf{e}_{θ_t} are in the West–East, South–North and wind direction, respectively.

The computed dune orientations, blue and red arrows in figure 6, are however depending on a large number of parameters, for which we took typical values for eolian desert on Earth. We therefore run a sensibility test by calculating the dune orientations for grain diameters ranging from $100 \mu\text{m}$ to $400 \mu\text{m}$ and the speed-up ratio from 0.1 to 10 (wedges on figure 6). We also checked the sensibility the transport law by repeating the process with the quadratic transport also used for comparison in Pähzt and Durán (2020), which led to no more than $n\%$ of variation with respect to (11).

319 References

- 320 Andreotti B, Fourriere A, Ould-Kaddour F, Murray B, Claudin P (2009) Gi-
321 ant aeolian dune size determined by the average depth of the atmospheric
322 boundary layer. *Nature* 457(7233):1120–1123
- 323 Andreotti B, Claudin P, Devauchelle O, Durán O, Fourrière A (2012) Bedforms
324 in a turbulent stream: ripples, chevrons and antidunes. *Journal of Fluid
325 Mechanics* 690:94–128
- 326 Bacik KA, Lovett S, Colm-cille PC, Vriend NM (2020) Wake induced long
327 range repulsion of aqueous dunes. *Physical review letters* 124(5):054,501
- 328 Belcher SE, Hunt JCR (1998) Turbulent flow over hills and waves. *Annual
329 Review of Fluid Mechanics* 30(1):507–538
- 330 Charru F, Andreotti B, Claudin P (2013) Sand ripples and dunes. *Annual
331 Review of Fluid Mechanics* 45:469–493
- 332 Courrech du Pont S (2015) Dune morphodynamics. *Comptes Rendus Physique*
333 16(1):118–138
- 334 Courrech du Pont S, Narteau C, Gao X (2014) Two modes for dune orientation.
335 *Geology* 42(9):743–746
- 336 Farr TG, Rosen PA, Caro E, Crippen R, Duren R, Hensley S, Kobrick M,
337 Paller M, Rodriguez E, Roth L, et al. (2007) The shuttle radar topography
338 mission. *Reviews of geophysics* 45(2)
- 339 Fourriere A, Claudin P, Andreotti B (2010) Bedforms in a turbulent stream:
340 formation of ripples by primary linear instability and of dunes by nonlinear
341 pattern coarsening. *Journal of Fluid Mechanics* 649:287–328
- 342 Gadal C, Narteau C, Courrech Du Pont S, Rozier O, Claudin P (2019) Incip-
343 ient bedforms in a bidirectional wind regime. *Journal of Fluid Mechanics*
344 862:490–516
- 345 Gunn A, Wanker M, Lancaster N, Edmonds DA, Ewing RC, Jerolmack DJ
346 (2021) Circadian rhythm of dune-field activity. *Geophysical Research Letters*
347 48(5):e2020GL090,924
- 348 Hersbach H, Bell B, Berrisford P, Hirahara S, Horányi A, Muñoz-Sabater
349 J, Nicolas J, Peubey C, Radu R, Schepers D, et al. (2020) The era5
350 global reanalysis. *Quarterly Journal of the Royal Meteorological Society*
351 146(730):1999–2049
- 352 Hesp PA, Smyth TAG, Nielsen P, Walker IJ, Bauer BO, Davidson-Arnott R
353 (2015) Flow deflection over a foredune. *Geomorphology* 230:64–74
- 354 Hunt JCR, Vilenski GG, Johnson ER (2006) Stratified separated flow around
355 a mountain with an inversion layer below the mountain top. *Journal of Fluid
356 Mechanics* 556:105–119
- 357 Jiang Q (2014) Applicability of reduced-gravity shallow-water theory to
358 atmospheric flow over topography. *Journal of the Atmospheric Sciences*
359 71(4):1460–1479
- 360 Lancaster LNSM J (1984) Climate of the central namib desert. *Madoqua*
361 1984(1):5–61
- 362 Lancaster N (1985) Winds and sand movements in the namib sand sea. *Earth
363 Surface Processes and Landforms* 10(6):607–619

- 364 Muñoz-Sabater J, Dutra E, Agustí-Panareda A, Albergel C, Arduini G, Bal-
365 samo G, Bousetta S, Choulga M, Harrigan S, Hersbach H, et al. (2021)
366 Era5-land: A state-of-the-art global reanalysis dataset for land applications.
367 Earth System Science Data Discussions pp 1–50
- 368 Pähzt T, Durán O (2020) Unification of aeolian and fluvial sediment transport
369 rate from granular physics. *Physical review letters* 124(16):168,001
- 370 Rubin DM, Hunter RE (1987) Bedform alignment in di-
371 rectioally varying flows. *Science* 237:276–278, DOI
372 <https://doi.org/10.1126/science.237.4812.276>
- 373 Seidel DJ, Zhang Y, Beljaars A, Golaz JC, Jacobson AR, Medeiros B (2012)
374 Climatology of the planetary boundary layer over the continental united
375 states and europe. *Journal of Geophysical Research: Atmospheres* 117(D17)
- 376 Sheridan PF, Vosper SB (2006) A flow regime diagram for forecasting lee
377 waves, rotors and downslope winds. *Meteorological Applications* 13(2):179–
378 195
- 379 Smith AB, Jackson DWT, Cooper JAG (2017) Three-dimensional airflow and
380 sediment transport patterns over barchan dunes. *Geomorphology* 278:28–42
- 381 Stull R (2006) 9 - the atmospheric boundary layer. In: Wallace JM, Hobbs
382 PV (eds) *Atmospheric Science* (Second Edition), second edition edn, Aca-
383 demic Press, San Diego, pp 375–417, DOI <https://doi.org/10.1016/B978-0-12-732951-2.50014-4>
- 385 Stull RB (1988) An introduction to boundary layer meteorology, vol 13.
386 Springer Science & Business Media
- 387 Sullivan PP, McWilliams JC (2010) Dynamics of winds and currents coupled
388 to surface waves. *Annual Review of Fluid Mechanics* 42:19–42
- 389 Tritton D (2012) *Physical fluid dynamics*. Springer Science & Business Media
- 390 Vosper SB (2004) Inversion effects on mountain lee waves. *Quarterly Journal*
391 of the Royal Meteorological Society: A journal of the atmospheric sciences,
392 applied meteorology and physical oceanography 130(600):1723–1748
- 393 Walker IJ, Hesp PA, Davidson-Arnott RG, Bauer BO, Namikas SL,
394 Ollerhead J (2009) Responses of three-dimensional flow to variations
395 in the angle of incident wind and profile form of dunes: Greenwich
396 dunes, prince edward island, canada. *Geomorphology* 105:127–138, DOI
397 [10.1016/j.geomorph.2007.12.019](https://doi.org/10.1016/j.geomorph.2007.12.019)

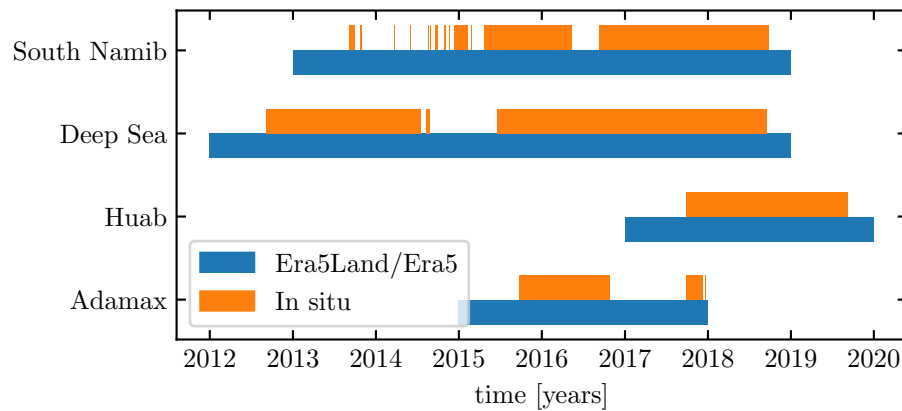


Fig. S1 Gant chart representing the valid time steps for the two data sets, for all stations.

398 **Supplementary Material for *Boundary-Layer Meteorology* Sample
399 Paper: Instructions for Authors**

400 **First Author* · Second Author · Third Author**

401 *Affiliation and email address for the corresponding author only (note that
402 the corresponding author does not need to be the first author).

404 **1. Shear velocity and calibration of the hydrodynamical roughness**

405 For each station, the hydrodynamic roughness is calibrated by finding the
406 one that minimizes the relative difference δ between the wind vectors of both
407 datasets:

$$\delta = \frac{\sqrt{\langle \|u_{*,era} - u_{*,station}\|^2 \rangle_t}}{\sqrt{\langle \|u_{*,era}\| \rangle_t \langle \|u_{*,station}\| \rangle_t}} \quad (15)$$

408 This δ -parameter is computed for hydrodynamic roughness values ranging
409 from 10^{-5} m to 10^{-2} m for the different stations. As shown by figure S3,
410 the minimum of δ in the space ($z_0,_{Era}, z_0,_{in situ}$) forms a line. We thus take
411 the roughness of the Era5Land dataset as the typical value when sediment
412 transport occurs, 10^{-3} m, corresponding to the thickness of the transport
413 layer (?). It leads for the Adamax, Deep Sea, Huab and South Namib stations
414 values of 2.7 mm, 0.76 mm, 0.12 mm and 0.48 mm, respectively.

415 The choice of the hydrodynamic roughness values only impacts the cal-
416 culated shear velocities, but note the wind directions. As such, most of our
417 conclusions are then independent of such a choice, and only the magnitude of
418 the wind velocity attenuation in confined situation might be affected.

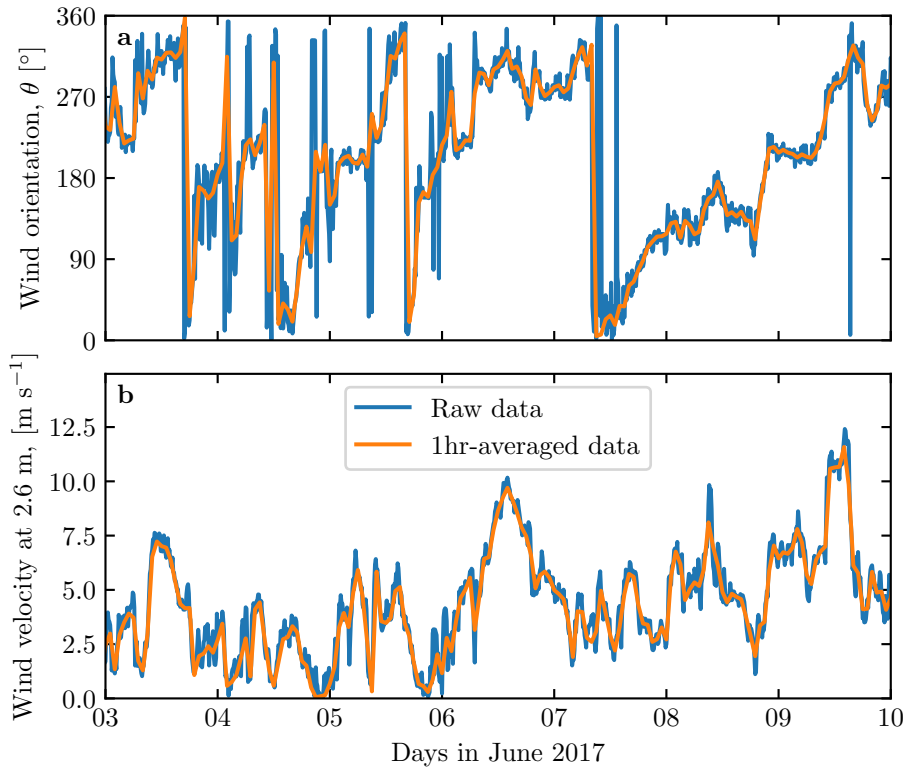


Fig. S2 Comparison between raw local wind measurements, and centered averaged data over one hour for the South Namib station. **a:** wind direction. **b:** wind velocity at the measurement height, 2.6 m.

419 2. Extraction of the ABL properties

420 In order to estimate the relevant non-dimensional numbers, one need to es-
 421 timate in addition to the wind and dune properties some parameters of the
 422 ABL. The Era5 dataset provides a direct bulk estimate of the ABL depth H
 423 from a bulk Richardson number calculation, as well as vertical profiles of the
 424 geopotential ϕ , temperature T and specific humidity e_w at given pressure lev-
 425 els P . From these quantities, the virtual potential temperature, which takes
 426 into account the vertical pressure and humidity changes, can be calculated as:

$$T_{vp} = T (1 + [R_M - 1] e_w) \left(\frac{P_0}{P} \right)^{P_c(1-0.24e_w)}, \quad (16)$$

427 where $P_0 = 10^5$ Pa is the standard pressure, $P_c = 0.2854$ the Poisson coefficient
 428 for dry air and $R_M = 1.61$ is the ratio between the molecular masses of dry
 429 air and water. The vertical coordinates are calculated as:

$$z = \frac{\phi R_t}{g R_t - \phi}, \quad (17)$$

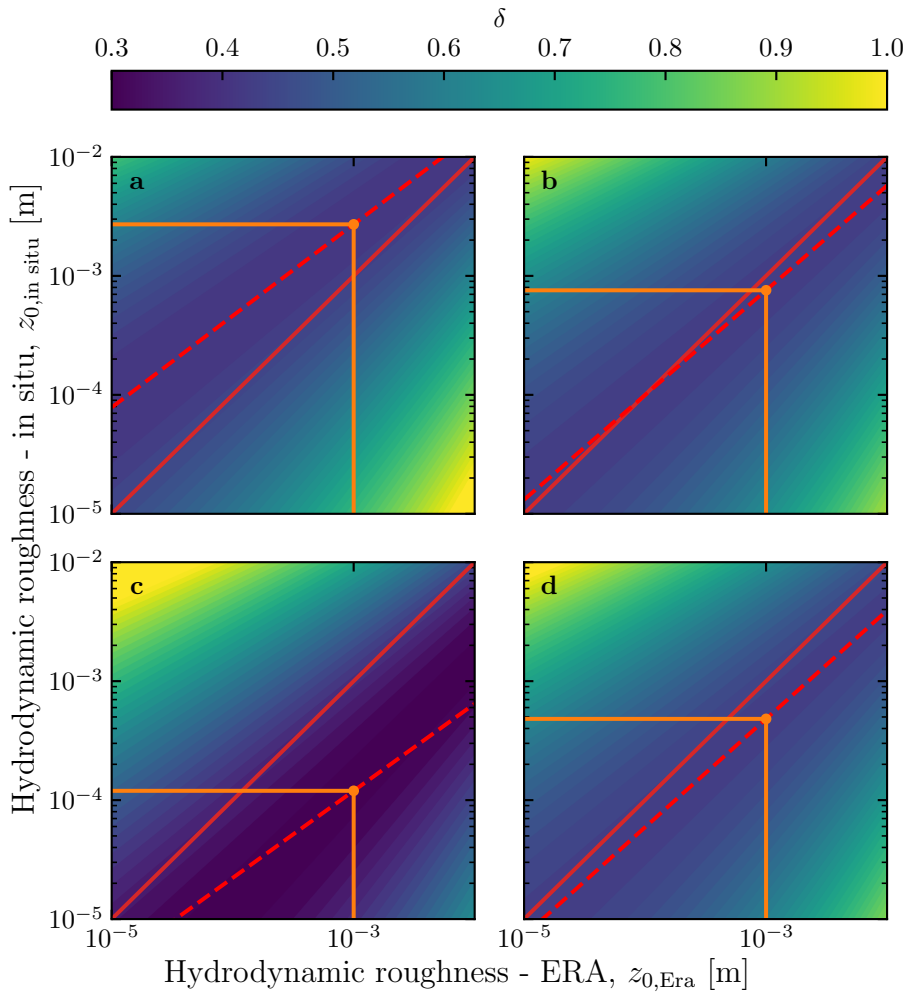


Fig. S3 Calibration of the hydrodynamic roughnesses. The metric δ defined in (15) is represented in colorscale as a function of the hydrodynamic roughnesses chosen for the Era5-Land and in situ datasets, for the Adamax (a), Deep Sea (b), Huab (c) and South Namib (d) Stations. The red dashed and plain lines shows the minima of δ and the identity line. The orange lines and dots highlight the chosen hydrodynamic roughnesses for the local datasets, by imposing $z_{0,\text{Era}} = 1 \text{ mm}$, leading for each station to 2.7 mm, 0.76 mm, 0.12 mm and 0.48 mm, respectively.

where $R_t = 6356766 \text{ m}$ is the average Earth radius, and $g = 9.81 \text{ m s}^{-2}$ the gravitational acceleration.

Example of obtained vertical profiles of the virtual potential temperature are shown in Fig. S9. On each of them, an average is computed below the ABL depth given by the Era5 dataset, and a linear function is fitted above.

Under the Boussinesq approximation, the temperature variations are assumed to induce most of those of the density, leading to $\Delta\rho/\rho \simeq \Delta T_{\text{vp}}/T_{\text{vp}}$.

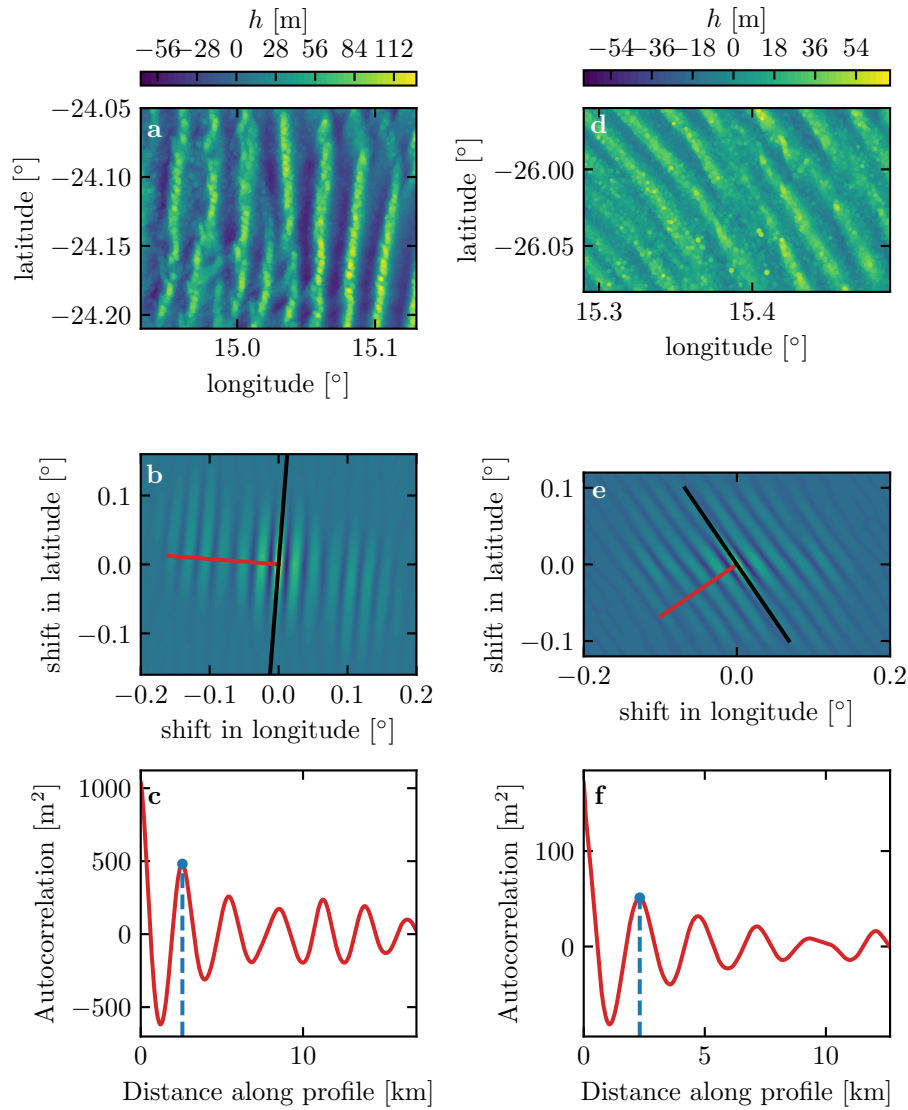


Fig. S4 Analysis of the DEMs of the Deep Sea (left column – **a**, **b**, **c**) and South Namib (right column – **d**, **e**, **f**) stations. **a–d**: Detrended topography (a second order polynomial is first fitted and then removed). **b–e**: autocorrelation matrix shown in colorscale. The black line shows the detected orientation, and the red line the profile along which the wavelength is calculated, shown in **c–f**. The blue lines and dots show the first peak of the autocorrelation profile, whose abscissa gives the characteristic wavelength of the dune pattern.

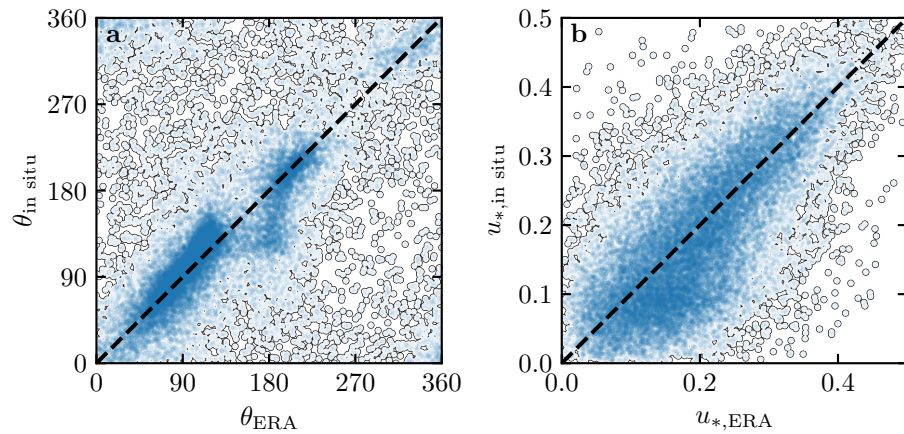


Fig. S5 Statistical agreement of the wind orientation (a) and velocity (b) between the Era5Land dataset and the local measurements for the Huab and Adamax stations. Note how the points are clustered around identity lines (dashed and black).

⁴³⁷ Here, $T_{\text{vp}}/T_{\text{vp}}$ is the relative virtual potential temperature jump at the capping,
⁴³⁸ directly measured on the vertical profiles.

⁴³⁹ Following Tritton (2012), the relative density jump at the capping layer

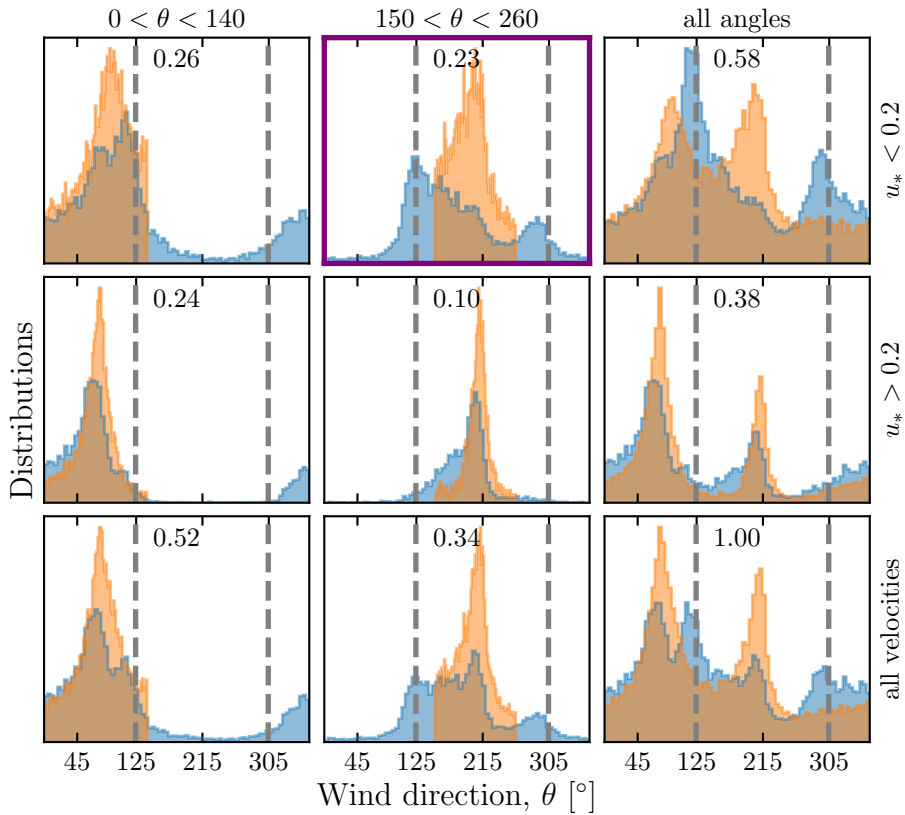


Fig. S6 Distributions of wind direction at the South Namib Station for the Era5Land climate reanalysis (orange) and the in situ measurements (blue). In each subplot, both distributions are plotted from the same time steps, selected with constraints on the wind direction (columns) and/or wind velocity (rows) in the Era5Land dataset. The grey dashed vertical lines indicate the dune orientation. The purple frame highlights the regime (small wind velocities, nocturnal summer wind) during which the wind data from both datasets differs. A similar figure can be obtained for the South Namib station (see Fig. 3).

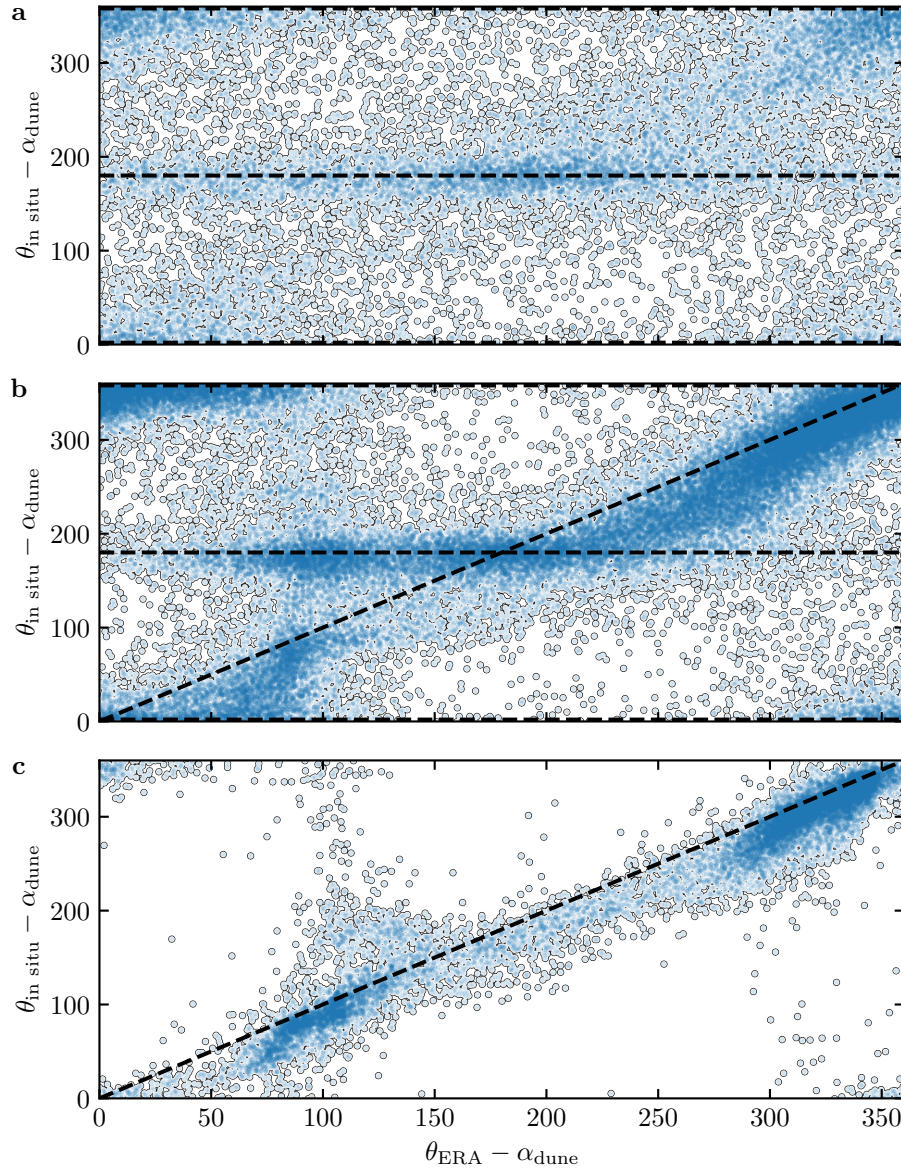


Fig. S7 Statistical comparison of the wind orientation between the Era5Land dataset and the local measurements for the South Namib and Deep Sea stations, for different velocity ranges. **a:** $u_{*,\text{ERA}} < 0.1 \text{ m s}^{-1}$. **b:** $0.1 < u_{*,\text{ERA}} \leq 0.25 \text{ m s}^{-1}$. **c:** $u_{*,\text{ERA}} \geq 0.25 \text{ m s}^{-1}$. Note that the measured dune orientations are subtracted to the wind orientation, which allows to plot both stations on the same graph. Black dashed lines indicate locally measured orientations aligned with the dune crests (here 0°, 180° and 360° – **a, b**), as well as the identity lines (**b, c**).

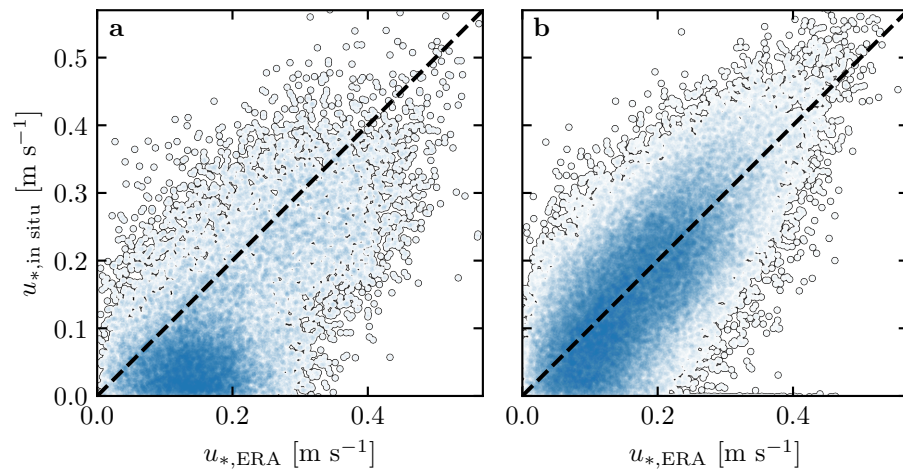


Fig. S8 Statistical comparison of the wind velocity between the Era5Land dataset and the local measurements for the South Namib and Deep Sea stations. **a:** Nocturnal summer easterly wind. **b:** Diurnal southerly wind. Black dashed lines are identity lines. The angle ranges used to select diurnal and nocturnal summer winds are those taken in Fig. 3 and Fig. S6.

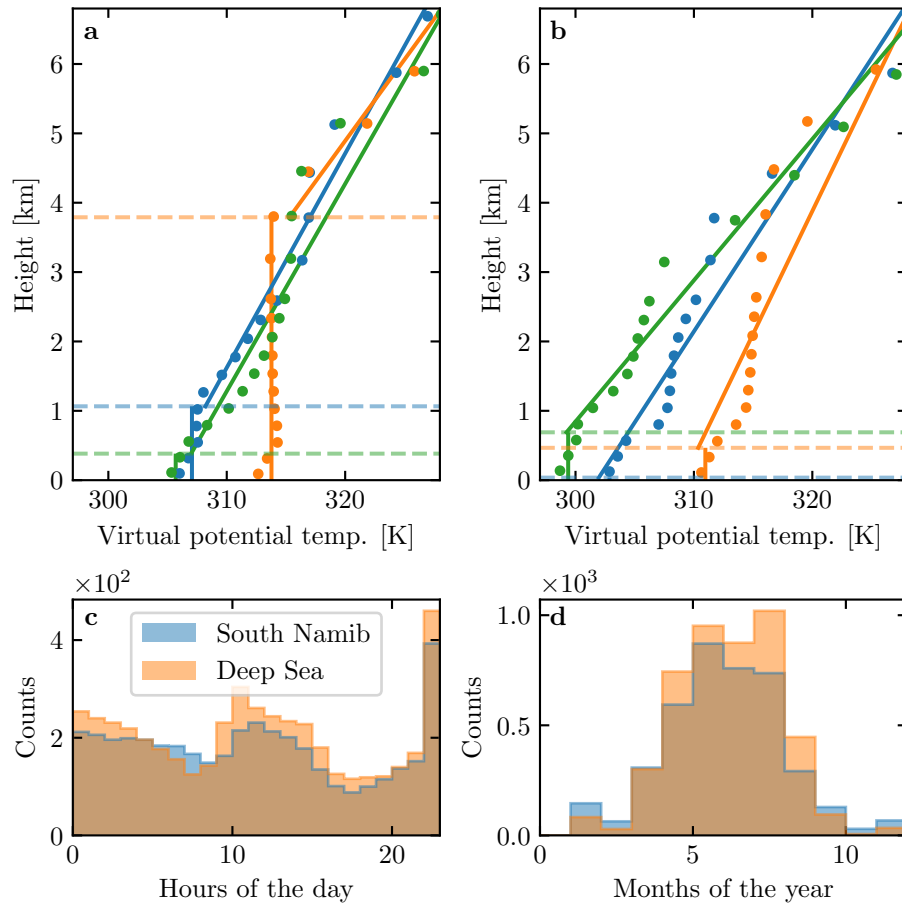


Fig. S9 **a:** Vertical profiles of the virtual potential temperature at 3 different time steps (blue - 29/11/2012 - 1100 UTC, orange - 21/03/2017 - 1200 UTC, green - 21/03/2017 - 2000 UTC) at the South Namib station. Dots: data from the ERA5 reanalysis. Transparent dashed lines: boundary layer height given by the ERA5 reanalysis, calculated from the bulk Richardson number (Seidel et al. 2012). Plain lines: vertical (boundary layer) and linear (free atmosphere) fits to estimate the quantities in Fig. S10. **b:** Examples of ill-processed vertical profiles at 3 different time steps (blue - 2/12/2013 - 2300 UTC, orange - 20/03/2017 - 0000 UTC, green - 14/07/2017 - 1400 UTC) at the South Namib station. **c:** Hourly distribution of ill-processed vertical profiles. **d:** Monthly distribution of ill-processed vertical profiles. These profiles are ill-processed because the temperature found at the boundary layer from the linear fit in the free-atm is smaller than the average one inside the boundary layer. This is an unstable situation, which does not allow to calculate the surface Froude number.

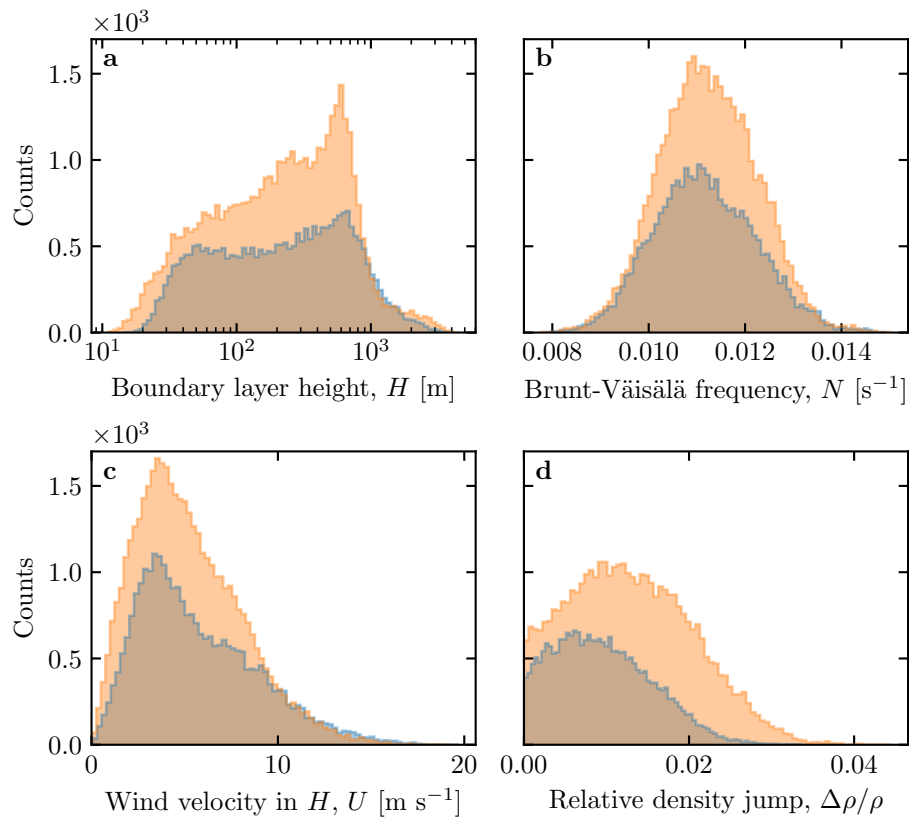


Fig. S10 Distributions of the meteorological parameters resulting from the processing of the Era5-Land data for the South Namib (blue) and the Deep Sea (orange) stations.

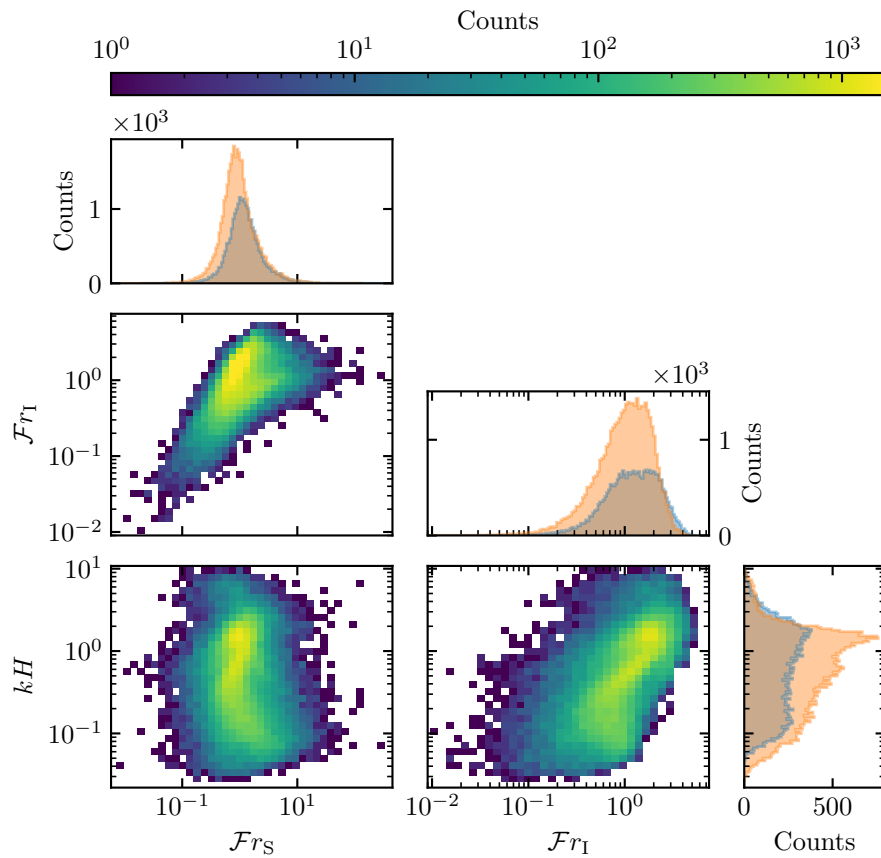


Fig. S11 Non-dimensional parameters distributions. For the marginal distributions, the orange correspond to the South Namib station, and the blue to the Deep Sea station.

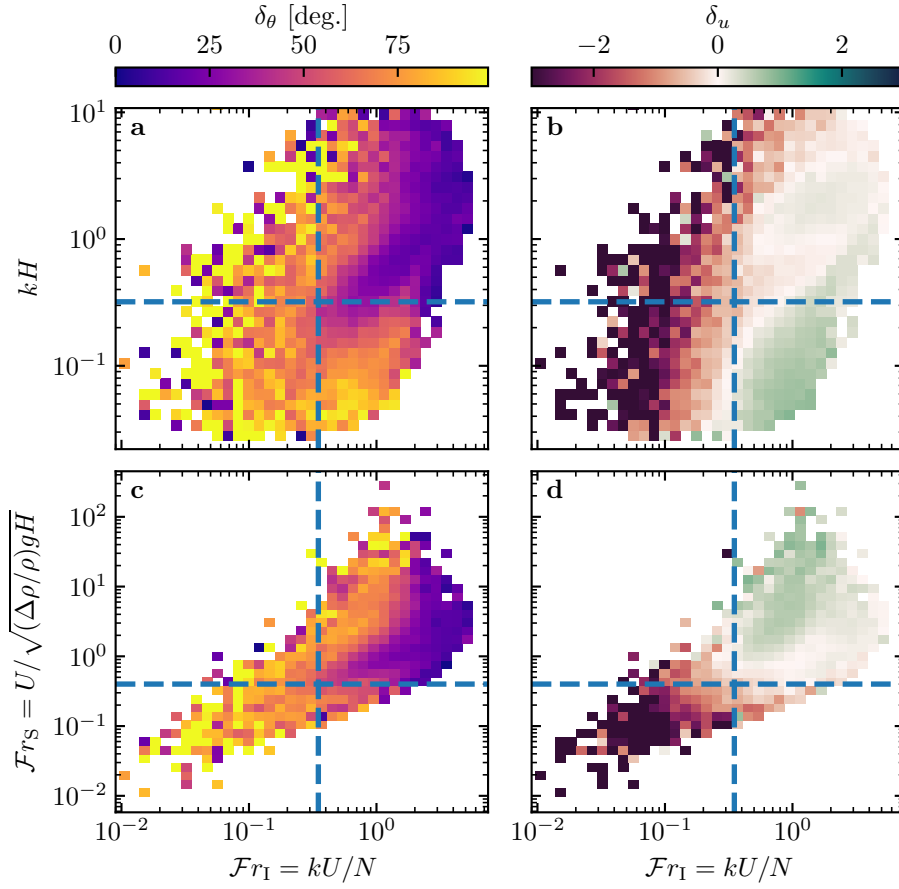


Fig. S12 Regime diagrams of the wind deviation δ_θ and relative attenuation/amplification δ_u in the spaces (\mathcal{Fr}_I, kH) and $(\mathcal{Fr}_I, \mathcal{Fr}_S)$, containing the data from both the Deep Sea and South Namib stations. Blue dashed lines empirically delimit the different regimes. The point density in each bin of the diagrams is shown in Fig. S11. The regime diagrams in the space (\mathcal{Fr}_S, kH) are shown in Fig. 5 of the main article.

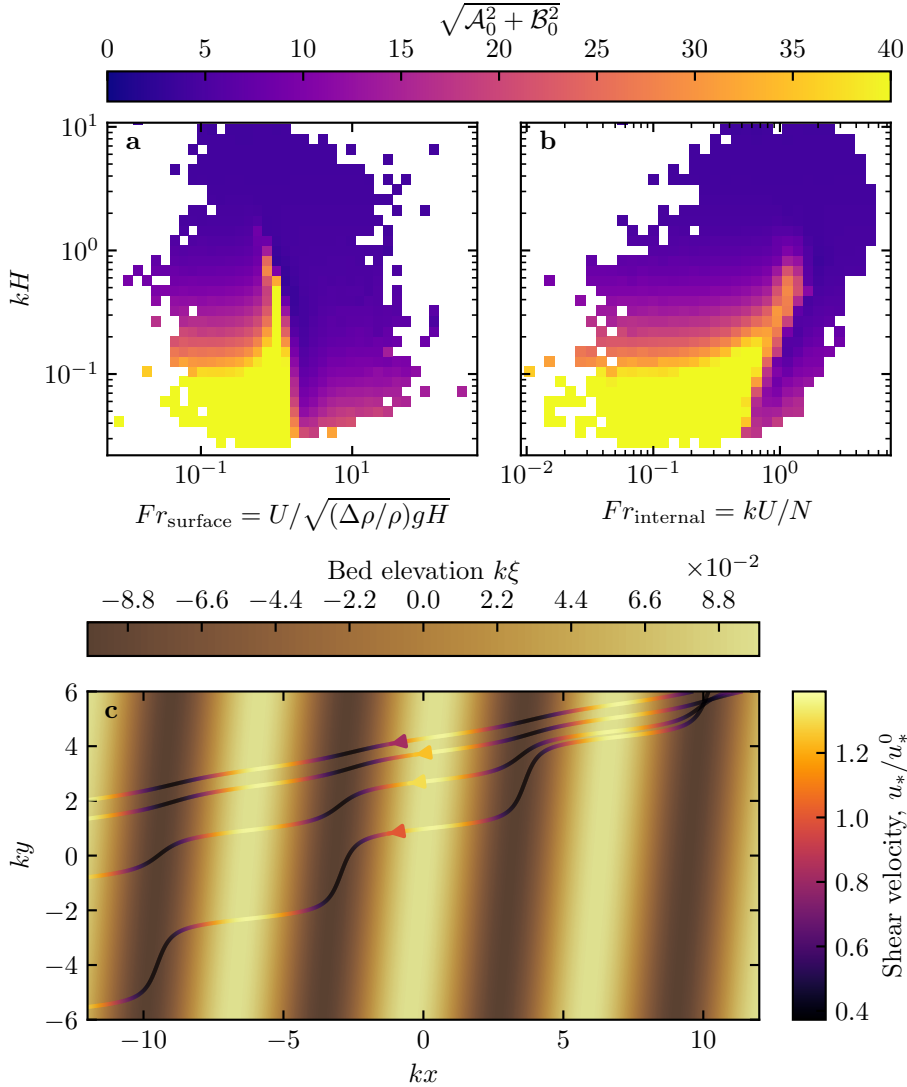


Fig. S13 Physical interpretation of the flow disturbance. (a) and (b) Magnitude of the disturbance induced by a sinusoidal topography calculated from the time series of the non-dimensional numbers presented in Figures 4 and 5 using the linear model of Andreotti et al. (2009). (c) Shear velocity streamlines represented in the case of the Deep Sea station, for increasing values of $\sqrt{\mathcal{A}_0^2 + \mathcal{B}_0^2}$. From the upper to the lower streamline, values of $(kH, Fr_{\text{surface}}, Fr_{\text{internal}}, \mathcal{A}_0, \mathcal{B}_0, \sqrt{\mathcal{A}_0^2 + \mathcal{B}_0^2})$ are $(1.9, 0.6, 1.5, 3.4, 1.0, 3.5)$, $(1.5, 0.3, 0.4, 4.8, 1.4, 5.0)$, $(0.1, 3.5, 1.0, 8.6, 0.1, 8.6)$, $(0.5, 0.05, 0.04, 9.6, 2.5, 9.9)$.